Petroleum Science 23 (2026) 7072–7085

Contents lists available at ScienceDirect

Petroleum Science

journal homepage: www.keaipublishing.com/en/journals/petroleum-science

Original Paper

Numerical investigation on T_1–T_2–based wettability in shale oil

Ji-Long Liu, Ran-Hong Xie *, Jiang-Feng Guo, Bo-Chuan Jin, Chong Deng

State Key Laboratory of Petroleum Resources and Engineering, China University of Petroleum (Beijing), Beijing 102249, China

ARTICLE INFO

Article history:
Received 7 January 2026
Received in revised form
23 March 2026
Accepted 13 May 2026
Available online 20 May 2026

Edited by Jie Hao

Keywords:
Shale oil
Mixed wetting
Water–wet proportion
Random walk

ABSTRACT

Wettability analysis in shale reservoirs is crucial for evaluating reserve assessment. Nuclear Magnetic Resonance (NMR) is a widely adopted non–destructive technique for characterizing wettability in porous media. However, the complex fluid behavior in shale oil poses challenges for traditional T_1–T_2–based wettability analysis. We developed a T_1–T_2 relaxation theory specifically in mixed–wettability shale oil, and calibrated the simulation parameters using experimental T_1–T_2 data from parallel core samples. Furthermore, we conducted numerical simulations of T_1–T_2 responses at varying conditions, including varying proportions of wetting regions, echo spacings (T_{E_S}), contact angles, and magnetic field frequencies (f). We investigated how magnetic field frequency affects T_1–T_2–derived petrophysical parameters in mixed wetting shale oil. The results show the effects of wettability and frequency on NMR measurements are significant. For example, at $T_E = 0.4$ ms, $f = 200$ MHz, and a water–wet region proportion of 0.78, the measured porosity (0.217%), T_{2LM} (0.354 ms), and T_{1LM} (27.1 ms) were 0.667 times, 1.79 times, and 2.33 times as high as those at a water–wet proportion of 0.52, respectively. This work provides a novel framework for understanding the frequency dependence of NMR petrophysical parameters in mixed–wetting shale oil, offering valuable insights for both laboratory measurements and well logging applications.

© 2026 The Authors. Publishing services by Elsevier B.V. on behalf of KeAi Communications Co. Ltd. This is an open access article under the CC BY-NC-ND license (http://creativecommons.org/licenses/by-nc-nd/4.0/).

1. Introduction

Petroleum is a vital energy source and plays a critical role in the national economy. With the advancement of hydraulic fracturing technology, unconventional shale oil resources have been accounting for an increasing proportion of total petroleum resources year by year (Gao et al., 2024). China has achieved notable progress in annual terrestrial shale oil production. However, its share in the country's total oil output remains very low. Consequently, intensifying exploration and development efforts for terrestrial shale oil has become urgent (Zhao et al., 2023; Zou et al., 2022, 2023; Mi et al., 2023). Shale oil is hosted in organic–rich shale reservoirs and consists of liquid hydrocarbons characterized by in–situ generation or short–distance migration. Its resource volume is primarily controlled by the abundance, type, and maturity of organic matter (Zou et al., 2013; Pang et al., 2023).

Shale oil, a significant unconventional energy resource, is predominantly stored in shale reservoirs with complex pore structures. Currently, three principal techniques are employed for wettability characterization in shale oil reservoirs: spontaneous imbibition, contact angle measurement, and nuclear magnetic resonance (NMR). Among these approaches, contact angle measurement offers operational simplicity and wide applicability, yet its effectiveness is substantially constrained when analyzing highly heterogeneous shale formations due to measurement inaccuracies. The spontaneous imbibition approach evaluates wettability by quantifying either the volume of fluid absorbed under spontaneous and forced conditions or the work required for fluid displacement within core samples. While this approach provides valuable insights into pore network connectivity and comparative wettability differences among core samples, it fails to yield absolute wettability values or detailed pore–scale fluid distribution information. In comparison, NMR techniques exhibit distinct advantages by employing T_1/T_2 relaxation time analysis. This approach enables non–destructive, non–invasive, and continuous wettability assessment, making it particularly suitable for downhole reservoir conditions. The NMR approach not only overcomes the limitations of conventional techniques but also

* Corresponding author
E-mail address: xieranhong@cup.edu.cn (R.-H. Xie).
Peer review under the responsibility of China University of Petroleum (Beijing).

https://doi.org/10.1016/j.petsci.2026.05.019
1995-8226/© 2026 The Authors. Publishing services by Elsevier B.V. on behalf of KeAi Communications Co. Ltd. This is an open access article under the CC BY-NC-ND license (http://creativecommons.org/licenses/by-nc-nd/4.0/).

provides comprehensive wettability characterization across various reservoir scales.

NMR methods, characterizing wettability of shale oil reservoirs, include numerical simulations and experimental methods. Experimental methods can directly determine reservoir wettability indices through NMR relaxation times, such as the Hirasaki wettability index (Hirasakl, 1991), Fleury wettability index (Fleury and Deflandre F, 2003), Chen wettability index (Chen et al., 2006), Al–Mahrooqi wettability index, Tandon wettability index, and AL–Garadi wettability index (Al–Mahrooqi et al., 2006; Tandon et al., 2020; Al–Garadi et al., 2022). The Hirasaki wettability index is determined by the fluid contact surface area and the surface relaxavity of each fluid component. The Fleury wettability index is determined by the fluid–pore contact area. The Chen wettability index, integrating the Hirasaki and Fleury indices, is determined by the effective surface relaxavity. Al–Mahrooqi wettability index, based on the capillary bundle model, is determined by T_2 measurements for bound water and residual oil states. The Tandon wettability index is derived from the product of the fluid contact surface area and fluid surface relaxavity, along with the difference in fluid surface relaxavity. However, these indices exhibit limitations when analyzing pores containing minimal non–wetting phases with blocky T_2 distributions. To address this, Al–Garadi et al. (2022) developed an enhanced wettability index incorporating bulk relaxation times under four saturation states, including water–saturated, oil–saturated, bound water, and residual oil conditions. The strong heterogeneity of shale reservoirs, manifested through variable organic matter distribution and mineral composition, poses significant challenges for NMR–based wettability characterization. Experimental studies demonstrate that increasing total organic carbon (TOC) content and thermal maturity promote wettability transition from water–wet to oil–wet states (Su et al., 2018; Wang et al., 2022), enhancing oil absorption during imbibition processes. Notably, Wang et al. (2018) established separate wettability indices for organic and inorganic pores through systematic NMR experiments, providing critical insights into shale's dual–porosity system. Current NMR–based investigations of shale oil wettability are predominantly confined to core–scale average measurements, failing to provide pore–scale resolution. While NMR numerical simulations offer the potential to address this limitation by isolating individual factors influencing NMR responses in mixed–wet systems, their development remains insufficient. These simulations could theoretically compensate for experimental shortcomings and elucidate fundamental T_1–T_2 response mechanisms in mixed–wet shale oil. However, the unclear NMR response behaviors in such complex systems pose substantial challenges for simulation–derived characterization methods. Both the relaxation theory and characterization methodologies for NMR–based shale wettability analysis were urgently needed to investigate. Brown and Fatt (1956) established that molecular dynamics at solid–liquid interfaces exhibit significantly slower kinetics compared to bulk liquid phases. This phenomenon reduces diffusion coefficients while enhancing nuclear magnetic relaxation rates for magnetically aligned ^{1}H nuclei, thereby facilitating more efficient energy transfer to the surrounding matrix. The extent of this effect is fundamentally governed by the relative wettability between the solid and liquid phases. Their seminal work demonstrated that wettability variations among sandstone reservoirs primarily stem from the proportional distribution of oleophilic or hydrophilic surface areas relative to the total interfacial area. Through systematic NMR experiments on unconsolidated sandstone cores with controlled wettability gradients (ranging from strongly water–wet to intermediate–wet states), the researchers validated NMR's capability for quantitative determination of wettability domain distributions in reservoirs. However, this methodology necessitates stringent measurement conditions, including a magnetically shielded environment, ultra–low noise instrumentation, and specialized radiofrequency coil configurations. The technical complexity and procedural demands of this approach ultimately limit its practical utility for routine laboratory wettability characterization. Kumar et al. (1969) introduced a breakthrough technique for wettability characterization in porous systems, demonstrating that water relaxation time measurements could reliably indicate wetting phase distribution. Notably, their system design utilizing conventional electromagnets and optimized circuitry achieved laboratory–grade results without expensive magnetic shielding, representing a major step toward practical NMR applications in petrophysics. Borgia et al. (1991) systematically investigated NMR responses in sandstone cores across multiple saturation states. Their experimental design encompassed water–saturated states, oil–displaced water phases, and residual oil saturation states. The researchers specifically analyzed T_1 relaxation behavior in both intermediate–wet and strongly water–wet cores, establishing critical baseline data for wettability interpretation through NMR measurements. Hsu et al. (1992) performed a systematic NMR relaxation study to investigate wettability alteration in carbonate rocks treated with cyclohexane acids. They used inversion recovery and spin–locking methods to measure T_1 and $T_{1\rho}$ of water–wet and chemically–induced oil–wet samples, followed by conventional Amott/USBM wettability measurements. The results indicate that proton (^{1}H) relaxation times can distinguish between water–wet and oil–wet surfaces, revealing significant sensitivity to paramagnetic impurities. Deuterium (^{2}H) T_1 is unaffected by changes in surface wettability. Deuterium $T_{1\rho}$ shows shorter relaxation times for water–wet systems and longer relaxation times for oil–wet systems, influenced by magnetic impurities. It is suggested that the spin–lattice relaxation mechanism of ^{1}H in H_2O differs from that of deuterium in D_2O. ^{1}H relaxation occurs through intra–molecular and inter–molecular dipole–dipole interactions, whereas deuterium in D_2O occurs primarily through intra-molecular quadrupole coupling. Bonalde et al. (1995) developed synthetic sandstone samples with controlled wettability heterogeneity by systematically blending water–wet quartz grains with phenolic resin binders. Employing inversion recovery (IR) pulse sequences, the researchers precisely measure longitudinal relaxation times (T_1) of both ^{1}H and deuterium nuclei. Their comprehensive analysis revealed that the spectral width of the relaxation rate distribution function and its characteristic stretching exponent (β) exhibit strong correlations with the intensity of surface interactions, the specific nature of molecular bonding at grain–fluid interfaces, and the effective permeability of the composite porous medium. As research advances in rock wettability characterization, it has become evident that wettability behavior is governed by multiple interdependent factors, including pore geometry, the spatial distribution of wetting phases across pore surfaces, adsorbed film thickness, and fluid saturation (Al–Mahrooqi et al., 2003, 2006; Howard, 1998; Guan et al., 2002). Looyestijn and Hofman (2006) developed a novel NMR–based wettability characterization method that correlates the microscopic spatial distribution of crude oil with surface–induced

relaxation enhancement at specific saturation states, establishing a quantitative relationship between fluid–rock interfacial interactions and wettability indices. Looyestijn (2008) successfully implemented this NMR–derived wettability assessment methodology in field–scale logging operations, demonstrating its robust applicability across diverse lithologies under varying wettability conditions. Building upon this foundation, Al–Muthana et al. (2012) established a specialized NMR wettability index for carbonate formations by integrating prior wettability constraints from core–scale experimental data with downhole NMR measurements. Chen et al. (2006) developed the innovative NMR–based wettability characterization method for Berea sandstone cores exposed to oil–based drilling muds containing surfactants, utilizing differential surface relaxation responses between water and oil phases under controlled partial saturation conditions. SayedAkram et al. (2016) pioneered a novel digital petrophysical approach by performing high–fidelity NMR numerical simulations on mixed–wet carbonate systems reconstructed from micro–CT images, with subsequent experimental validation demonstrating excellent agreement between simulated and measured NMR responses. Sulucarnain et al. (2012) experimentally demonstrated through systematic T_2 relaxation analysis of organic–rich Ordovician shale samples that surface relaxation dominates the NMR response. Liang et al. (2019) established through systematic NMR measurements that wetting phases in porous media exhibit significantly higher T_1/T_2 ratios compared to non–wetting phases, providing a quantitative indicator for wettability assessment. Building on this foundation, Valori et al. (2017) further validated the robust correlation between T_1/T_2 ratios and wettability states in oil–saturated reservoir rocks at varying saturation. In their subsequent critical review, Valori et al. (2018) comprehensively evaluated the advantages and limitations of field cycling techniques, saturation–based techniques, T_1/T_2–based techniques, and restricted diffusion–based techniques for characterizing rock wettability, emphasizing the persistent challenge of developing a universal wettability quantification methodology for heterogeneous reservoir systems. Newgord et al. (2020) systematically evaluated wettability states in mixed–wet rocks under controlled partial saturation conditions through integrated fluid displacement experiments coupled with multi–dimensional NMR measurements (T_2, D–T_2, and T_1–T_2), establishing robust correlations between fluid distribution patterns and surface wettability. Tandon et al. (2020) developed a digital petrophysical framework combining micro–CT–based pore network modeling with finite volume simulations to quantify pore–scale wettability indices in both water–wet and hydrocarbon–wet sandstone/carbonate systems. Based on the research by Looyestijn et al., Dick et al. (2022) established a wettability index model suitable for unconventional reservoirs saturated with oil and water exhibiting multi–peak distribution characteristics. Liang et al. (2023) used the random walk method to simulate the T_2 responses of pore fluids in tight sandstones, however, there was a significant discrepancy between the digital rock models and actual reservoirs. Liu et al. (2025a) developed a T_1–T_2 relaxation theory and numerical simulation method for shale oil reservoirs with complex mineralogical compositions. Based on the assumption that organic pores are fully saturated with oil while inorganic pores are fully saturated with water, they investigated the effects of magnetic field frequency, pyrite content, clay mineral content, and clay mineral type on the T_1–T_2 responses of shale oil reservoirs. Furthermore, they established a frequency–conversion cross–plots for shale oil reservoirs that incorporates organic–pore oil, inorganic–pore water, clay–bound water, and organic matter saturation, accounting for the influences of the aforementioned factors.

Current research on NMR–based wettability characterization in shale oil reveals four deficiencies: (1) the fundamental relaxation mechanisms underlying two–dimensional NMR (T_1–T_2) responses remain poorly understood, particularly at nanoscale pore interfaces; (2) existing numerical simulations fail to incorporate authentic shale reservoir conditions, lacking realistic pore geometries and organic matter distributions from actual samples; (3) quantitative models for interpreting two–dimensional NMR signatures in finely heterogeneous, mixed–wet shale reservoirs are notably absent; and (4) no comprehensive methodology exists to account for frequency–dependent variations when converting NMR–derived petrophysical parameters in mixed–wet shale reservoirs, significantly limiting the technique's field applicability.

The NMR relaxation mechanisms in mixed–wet shale oil were proposed in this paper and the T_1–T_2 numerical investigations in mixed–wet shale oil were introduced. Unlike traditional theory, this relaxation theory focuses on elucidating the frequency–dependent characteristics of pore fluid relaxation parameters. On this basis, the T_1–T_2 numerical simulation framework was constructed, including the T_1–T_2 numerical simulation based on fluid distribution models. The digital core technology in mixed–wet shale oil was combined with NMR experiments to determine transverse surface relaxavity. The random walk was used for the T_1–T_2 responses simulation in mixed–wet shale oil at different magnetic field frequencies, proportions of water–wet regions (PWRs), echo spacings (T_{Es}), and wetting angles. The T_1–T_2–based petrophysical parameters frequency conversion cross–plots in mixed–wet shale oil were established.

2. Theory

2.1. T_1–T_2 relaxation theory

Based on the distribution characteristics of oil and water in inorganic pores, we established the NMR relaxation theory, which includes expressions for organic matter, oil and water (Liu et al., 2024a, 2024b, 2024c; Tandon and Heidari, 2019; Singer et al., 2020):

$$\begin{cases} \dfrac{1}{T_{1L}} = \dfrac{1}{T_{1B,L}} + \dfrac{1}{T_{1S,L}} \\ \dfrac{1}{T_{1K}} = \dfrac{1}{T_{1B,K}} \\ \dfrac{1}{T_{2L}} = \dfrac{1}{T_{2B,L}} + + \dfrac{1}{T_{2S,L}} + \dfrac{1}{T_{2D,L}} \\ \dfrac{1}{T_{2K}} = \dfrac{1}{T_{2B,K}}, \end{cases} \tag{1}$$

where, water or oil can be represented by subscript L, and the organic matter can be represented by subscript K. The $T_{1,K}$ and T_{2K} represent the longitudinal and transverse relaxation time of organic matter. $T_{1B,K}$, and $T_{2B,K}$ represent the longitudinal and transverse bulk relaxation time. The $T_{1B,L}$ and $T_{2B,L}$ in Eq. (1) can be

$$\begin{cases} \dfrac{1}{T_{1B,L}} \approx \dfrac{3}{20}\left(\dfrac{\mu_0}{4\pi}\right)^2 \gamma^4 \hbar^2 \dfrac{1}{N} \sum_{i=1}^{N} \sum_{j!=i}^{N} \dfrac{k}{r_{ij}^6} \left[g\left(0, \tau_{R,L}, \tau_{l,L}\right) + 4g\left(2\omega, \tau_{R,L}, \tau_{l,L}\right) \right] \\ \dfrac{1}{T_{2B,L}} \approx \dfrac{3}{20}\left(\dfrac{\mu_0}{4\pi}\right)^2 \gamma^4 \hbar^2 \dfrac{1}{N} \sum_{i=1}^{N} \sum_{j!=i}^{N} \dfrac{k}{r_{ij}^6} \left[\dfrac{3}{2} g\left(0, \tau_L, \tau_{l,L}\right) + \dfrac{5}{2} g\left(\omega, \tau_L, \tau_{l,L}\right) + g\left(2\omega, \tau_L, \tau_{l,L}\right) \right] \\ \tau_L = \dfrac{4\pi}{3K_B} R_{R,L}^3 \dfrac{\eta_L}{T} \\ g\left(\omega, \tau_{R,L}, \tau_{l,L}\right) = \left(\left(1 - s_L^2\right) \dfrac{2\tau_{R,L}}{\left(1 + \omega\tau_{R,L}\right)^2} + s_L^2 \dfrac{2\tau_{l,L}}{\left(1 + \omega\tau_{l,L}\right)^2} \right), \end{cases} \tag{2}$$

described by Tandon et al. They represent the longitudinal and transverse bulk relaxation time ($T_{1B,L}$ and $T_{2B,L}$) for oil and water, and they can be represented as:

where, μ_0, γ, $\hbar$, K_B, ω, and T represent vacuum permeability, gyromagnetic ratio, reducing planck's constant, boltzmann's constant, angular frequency and temperature. r_{ij} represents the distance from ith and the jth ^{1}H. $g\left(\omega, \tau_{R,L}, \tau_{l,L}\right)$ represents the spectral density function for water or oil. $\tau_{R,L}$ and $\tau_{l,L}$ represent rotation related time from water and oil molecules and the ^{1}H nuclei in water and oil molecules. $R_{R,L}$ represents radius of rotation for oil and water. k represents the number of nearest protons. s_L represents generalized order parameter from L–S model (Lipari and Szabo, 1982). η_L represents the viscosity of oil or water.

Similar to the L–S model, the B–P–P model can be described by $T_{2TB,L}$ (Liu et al., 2024a; Tandon and Heidari, 2019). The P model can be described by $T_{1B,K}$ and $T_{2B,K}$ (Tandon and Heidari, 2019).

The $1/T_{2D,L}$ in Eq. (1) represents the diffusion relaxation rate for oil or water, respectively. It is related to the diffusion coefficients (D_L), echo spacing (T_E), internal magnetic field gradient (G_z), and gyromagnetic ratio (γ), which can be expressed as:

$$\frac{1}{T_{2D,L}} = \frac{D_L(\gamma G_z T_E)^2}{12}, \tag{3}$$

where G_z in Eq. (3) is related to the magnetic field frequency, and it can be described by the magnetic dipole theory (Liu et al., 2024a). It should be noted that the effects of pore scale need to be considered during the calculations.

The $1/T_{2S,L}$ and $1/T_{1S,L}$ represent transverse and longitudinal surface relaxation rates for oil or water, respectively. They are shown as:

$$\begin{cases} \dfrac{1}{T_{1S,W}} = f_1^W \cdot \tau_{m,W} \cdot K_{2D}^1\left(\tau_{m,W}, \tau_{s,W}, \omega_I, \omega_s\right) \\ \dfrac{1}{T_{2S,W}} = f_2^W \cdot \tau_{m,W} \cdot K_{2D}^2\left(\tau_{m,W}, \tau_{s,W}, \omega_I, \omega_s\right) \\ \dfrac{1}{T_{1S,O}} = f_1^O \cdot \sqrt{\tau_{m,O} \cdot \tau_{s,O}} \cdot K_{2D}^1\left(\tau_{m,O}, \tau_{s,O}, \omega_I, \omega_s\right) \\ \dfrac{1}{T_{2S,O}} = f_2^O \cdot \sqrt{\tau_{m,O} \cdot \tau_{s,O}} \cdot K_{2D}^2\left(\tau_{m,O}, \tau_{s,O}, \omega_I, \omega_s\right), \end{cases} \tag{4}$$

where, f_1^W, f_2^W, f_1^O, and f_2^O are parameters related to pore structure and fluid properties. $\tau_{m,O}$, $\tau_{m,W}$, and $\tau_{s,O}$, $\tau_{s,W}$ are the translation correlation times and surface residence times for oil and water, respectively. ω_s and ω_I represent angular frequencies representing paramagnetic ions and ^{1}H, respectively.

It is assumed that cylindrical pore (Liu et al., 2024a), the longitudinal and transverse surface relaxavities for oil and water are acquired as:

$$\begin{cases} \rho_{1S,W} = H_1^W \cdot \tau_{m,W} \cdot K_{2D}^1\left(\tau_{m,W}, \tau_{s,W}, \omega_I, \omega_s\right) \\ \rho_{2S,W} = H_2^W \cdot \tau_{m,W} \cdot K_{2D}^2\left(\tau_{m,W}, \tau_{s,W}, \omega_I, \omega_s\right) \\ \rho_{1S,O} = H_1^O \cdot \sqrt{\tau_{m,O} \cdot \tau_{s,O}} \cdot K_{2D}^1\left(\tau_{m,O}, \tau_{s,O}, \omega_I, \omega_s\right) \\ \rho_{2S,O} = H_2^O \cdot \sqrt{\tau_{m,O} \cdot \tau_{s,O}} \cdot K_{2D}^2\left(\tau_{m,O}, \tau_{s,O}, \omega_I, \omega_s\right), \end{cases} \tag{5}$$

where $f_1^W = H_1^W \cdot \frac{d}{2}$, $f_2^W = H_2^W \cdot \frac{d}{2}$, $f_1^O = H_1^O \cdot \frac{R}{2}$, $f_2^O = H_2^O \cdot \frac{R}{2}$. The NMR response in shale oil can be simulated based on three–dimensional multicomponent digital core reconstructions of fluid distributions.

2.2. Simulation method

The random walk (RW) method has been employed for one–dimensional NMR numerical simulation in shale oil (Liu et al., 2024a, 2024b, 2024c). Based on previously digital shale cores (Liu et al., 2024b), we utilized the RW method to simulate SR–CPMG pulse sequences. During T_1 editing and T_2 measurement sequences, hydrogen nuclei in oil or water undergo inelastic collisions with pore surfaces, and the corresponding signal amplitudes can be shown as:

$$\begin{cases} AMP_1 = AMP_{ori} \cdot \left(1 - \dfrac{2}{3} \cdot \dfrac{\rho_{1S,L} r}{D} \cdot 0.96\right) \\ AMP_2 = (1 - AMP_1) \cdot \left(1 - \dfrac{2}{3} \cdot \dfrac{\rho_{2S,L} r}{D} \cdot 0.96\right), \end{cases} \tag{6}$$

In addition, effected by the heterogeneous internal magnetic field gradients, the hydrogen nuclei undergo diffusive motion, which can be represented as:

$$M_D(t) = M_{D_0} \cdot \frac{1}{K} \sum_{k=1}^{K} \exp\left(i\gamma G \int_0^t z^k(\tau) d\tau\right), \tag{7}$$

where M_{D_0} is the original amplitude of ^{1}H.

The expression for the phase decay of the CPMG is obtained as:

$$M_D(t) = \frac{1}{K}\sum_{k=1}^{K}\exp\left(i\gamma G\int_0^t z^k(\tau)\mathrm{d}\tau\right), \tag{8}$$

During CPMG pulse sequence simulations, the diffusion–induced magnetization decay of individual spins can be quantified through cosine–phase analysis, and it can be expressed as:

$$M_D(t) = \frac{1}{K}\sum_{i=1}^{K}\cos(\phi_i(t)), \tag{9}$$

The fluid particle phase should be reversed at $(1/2 + n)\cdot T_E$. For the i–th proton (^{1}H) at each time step, the generated phase can be expressed as:

$$\begin{aligned}\phi_1(t+\Delta t) = \phi_1(t) + \gamma G_z\cdot\left(\frac{z(t+\Delta t)+z(t)-2z(0)}{2}\right)\cdot\Delta t \\ +\gamma G_z\cdot\sqrt{\frac{D\cdot\Delta t^3}{6}}\cdot Normal(\,),\end{aligned} \tag{10}$$

where $z_0(t+\Delta t)$, $z_0(t)$, and $z_0(0)$ are the initial position of ^{1}H in digital shale core at the $t+\Delta t$, t, and initial time. $Normal()$ is the Gaussian random function.

On this basis, we can acquire the echo for oil and water as:

$$\begin{aligned}b(t,L) = porosity\cdot S_L\cdot HI_L\cdot\left(\frac{1}{N}\sum_{i=1}^{N}AMP_{2,i,L}\cdot\cos\left[AMP_{D_{i,L}}(t)\right]\cdot\exp\right. \\ \left.\left(-\frac{j\cdot T_E}{T_{2B,L}}\right)\right),\end{aligned} \tag{11}$$

where S_L represents the saturation of oil or water. HI_L represents the hydrogen index of oil or water.

3. Construction of fluids distribution

3.1. Research ideas and processes

By integrating pore–scale wettability modeling with T_1–T_2 relaxation theory, we elucidate the NMR response mechanisms in mixed–wettability shale oil. As illustrated in Fig. 1, our methodology employs a representative sub–volume (200 × 200 × 200 voxels, 3.9 μm^3 physical dimension) extracted from a multi–component digital shale core to optimize computational efficiency (Liu et al., 2023, 2024b). It should be noted that the inorganic porosity of the extracted shale sub–core is 0.77%, and the organic porosity is 2.78%.

The fluid dynamics within inorganic pores under coupled cohesive–viscous forces were simulated using the D_3Q_{19} lattice Boltzmann method (LBM), with boundary conditions constrained by pore network geometry, mineral spatial distribution, and organic–inorganic interfacial forces (Liu et al., 2024b). Through numerical solutions, we resolved three–dimensional fluid phase distributions across varying water–wet region proportions (PWRs) and contact angles (Fig. 1(a)). Consistent with the mixed–wettability T_1–T_2 relaxation theory presented in Section 2.2, three distinct relaxation mechanisms were identified: (i) bulk relaxation dominated by intramolecular and intermolecular dipole–dipole coupling, (ii) surface relaxation primarily governed by heteronuclear dipole interactions between fluid protons and paramagnetic sites, and (iii) diffusion relaxation modulated by internal magnetic field gradients. These mechanisms were quantitatively parameterized through T_1–T_2 experimental calibration from parallel core samples, enabling accurate simulation of NMR responses in multicomponent digital shale samples (Fig. 1(c)). Consequently, we employed random walk algorithms to simulate T_1–T_2 responses for varying PWRs and contact angles through numerical solutions of Eqs. (6)–(11). We acquired the resultant T_1–T_2 distributions by echo–train inversion, and quantitatively characterized fluid dynamics in mixed–wettability shale oil. It contributed to the establishment of petrophysical conversion models that account for heterogeneous wettability, as demonstrated in Fig. 1(b).

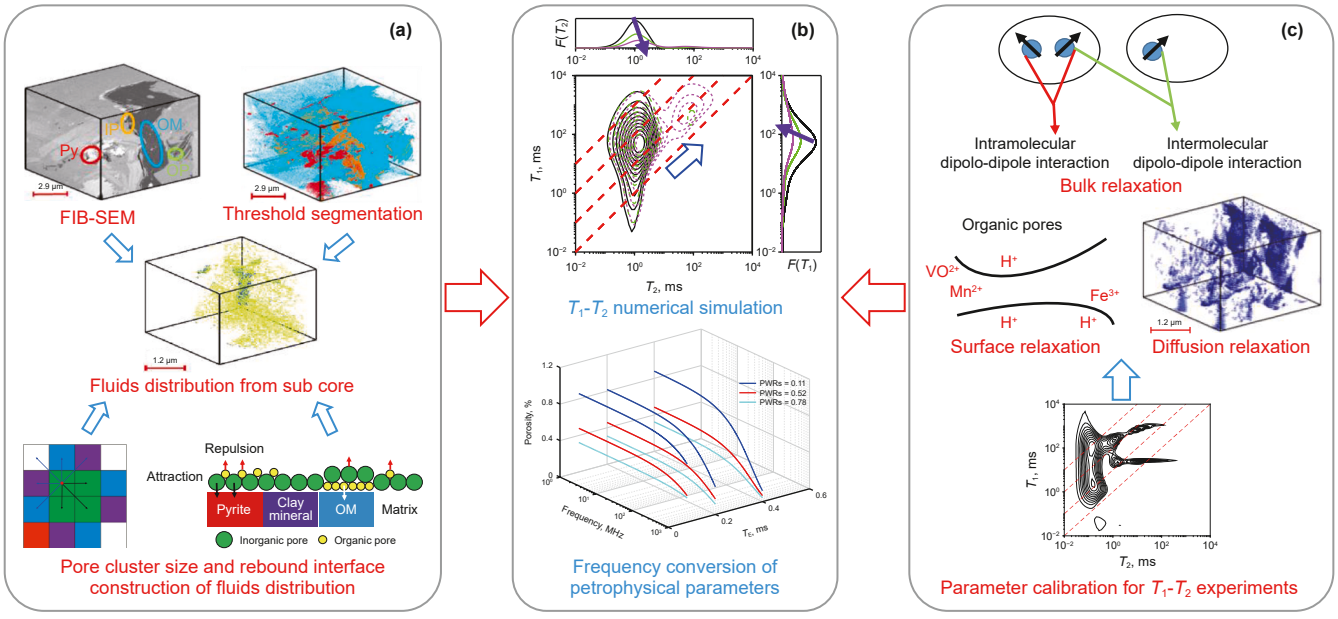


Fig. 1. Schematic diagram of the research.

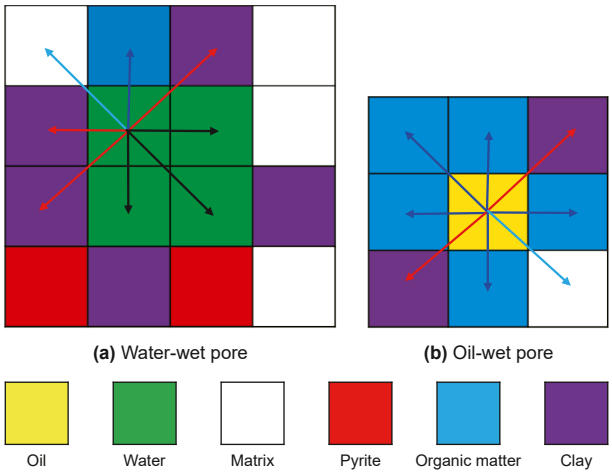


Fig. 2. Schematic diagram of fluid distribution construction. The red, blue, and light blue arrows represent the fluid migration paths prior to collision with clay minerals, organic matter, and the rock matrix, respectively. The black arrow specifically denotes the fluid path moving to the next pore location.

3.2. Construction process

To elucidate the proposed method for constructing three–dimensional fluid distribution, we demonstrate the construction process through a representative two–dimensional cross–section of the digital shale core. Here, it should be noted that we assume pores larger than a certain threshold are water–filled, while those smaller than the threshold are oil–filled. Fig. 2(a) and (b) schematically depict fluid dynamics under cohesive and viscous forces within small and large pore clusters, respectively. The simulations employ half–bounce boundary conditions to model nine–directional fluid movement along pore perimeters, where fluid particles rebound upon encountering organic matter, matrix, clays, or pyrite. These visualizations reveal how collision probabilities with different pore constituents (organic matter and mineral surfaces) and pore cluster size collectively govern local wettability states. Fig. 2 depicts scenarios of fluid collision with organic matter or minerals during fluid flow, where the collision probability and pore cluster size determine the local wettability of the pores. In Fig. 2(a), mineral–dominated collisions combined with pore cluster size exceeding the critical threshold establish water–wet conditions. Conversely, Fig. 2(b) shows organic–matter–preferential collisions in sub–threshold pore clusters creating oil–wet conditions. This wettability assignment methodology effectively captures the pore–scale fluid distribution heterogeneity in mixed–wet shale oil.

Based on fluid wettability simulation theory, the distribution characteristics of fluids on shale pore surfaces are influenced by pore size, cohesive forces within the fluids, and the interactions between fluids and mineral surfaces. These characteristics, as depicted for various pore cluster sizes, are presented in Fig. 3. The results indicate that minerals such as pyrite exhibit a higher affinity towards water, thereby promoting water–wet conditions on the pore surfaces. In contrast, organic matter shows a greater affinity for oil, leading to oil–wet pore surfaces.

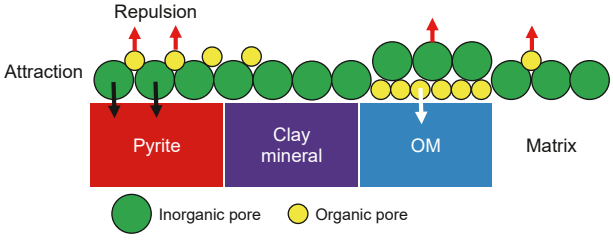


Fig. 3. Dynamics and wettability characterization for shale pore surface.

Adopting a similar methodology, the D_3Q_{19} model from the Lattice Boltzmann Method (LBM) was utilized for pore–scale wettability simulations (Liu et al., 2024b). As the pore–scale wettability theory, Fig. 4 depicts digital cores representing various proportions of water–wet regions and different contact angles. During simulations, we adjusted the threshold of pore cluster size and marked the boundary wettability of each pore cluster. We constructed multi–component digital shale cores with varying proportions of water–wet regions (PWRs) and contact angles within a three–dimensional pore space. The findings reveal that an increase in the proportion of water–wet regions results in greater pore space occupancy by water, with voxel counts of 11,805, 34,684, and 49,451 for these regions. In contrast, variations in contact angle did not significantly alter voxel counts of digital shale core with varying contact angles, which remained relatively constant at 11,799, 11,801, and 11,805, respectively. The proportion of voxels with changes relative to the total number of voxels in the original digital core is less than 0.1%. It should be noted that the contact angle referred to in this paper is a macroscopic result obtained by weighting and averaging the wetting–region proportions and contact angles of all pore clusters in the multi–component digital shale core, followed by summation.

4. Numerical simulations

Compared with experiments, numerical simulations can quantify the influence of individual factors on the NMR responses.

4.1. Parameters determination and results validation

Instruments operating at a 0.5 T magnetic field frequency are more effective for identifying the various fluid components in shale oil samples. To verify the accuracy of NMR relaxation theory in section 2, T_1–T_2 experimental measurements were performed on a shale sample (#AA–2) using the MesoMR23–060H–I instrument (Niumag, China), operating at a magnetic field strength of 0.5 T and a central frequency of 21.36 MHz. The measurements employed an inversion recovery–Carr–Purcell–Meiboom–Gill (IR–CPMG) pulse sequence with parameters: T_E of 0.08 ms, 2000 echoes, and a measurement environment temperature of approximately 25 °C. Following data acquisition, the T_1–T_2 distribution was obtained by inversion (Butler et al., 1981), as shown in Fig. 5(a). In Fig. 5(a), the transverse and longitudinal relaxation times for organic matter are 0.12 ms and 150 ms, respectively. For oil, these values are 3.73 ms and 464.16 ms, and for water, they are 1.55 ms and 21.5 ms, respectively. Utilizing the NMR relaxation mechanisms and fluid distribution within inorganic pores, the random walk method was applied to simulate T_1–T_2 responses with PWR = 0.11. The numerical and experimental results have good consistency in Fig. 5(b). It should be noted that the digital core in this study characterizes the pore size distribution of smaller pores, whereas the T_1–T_2 measurements from plug sample cover a broader range of pore sizes, resulting in certain discrepancies between the two. To validate the accuracy of the simulation results, the spectral peak of the simulated organic pore oil aligns with the central region of the two organic pore oil signals observed in the plug sample T_1–T_2 spectra, and the range of the simulated organic pore oil spectral peak covers the pore size range characterized by the T_1–T_2 measurements from plug sample. The T_2 and

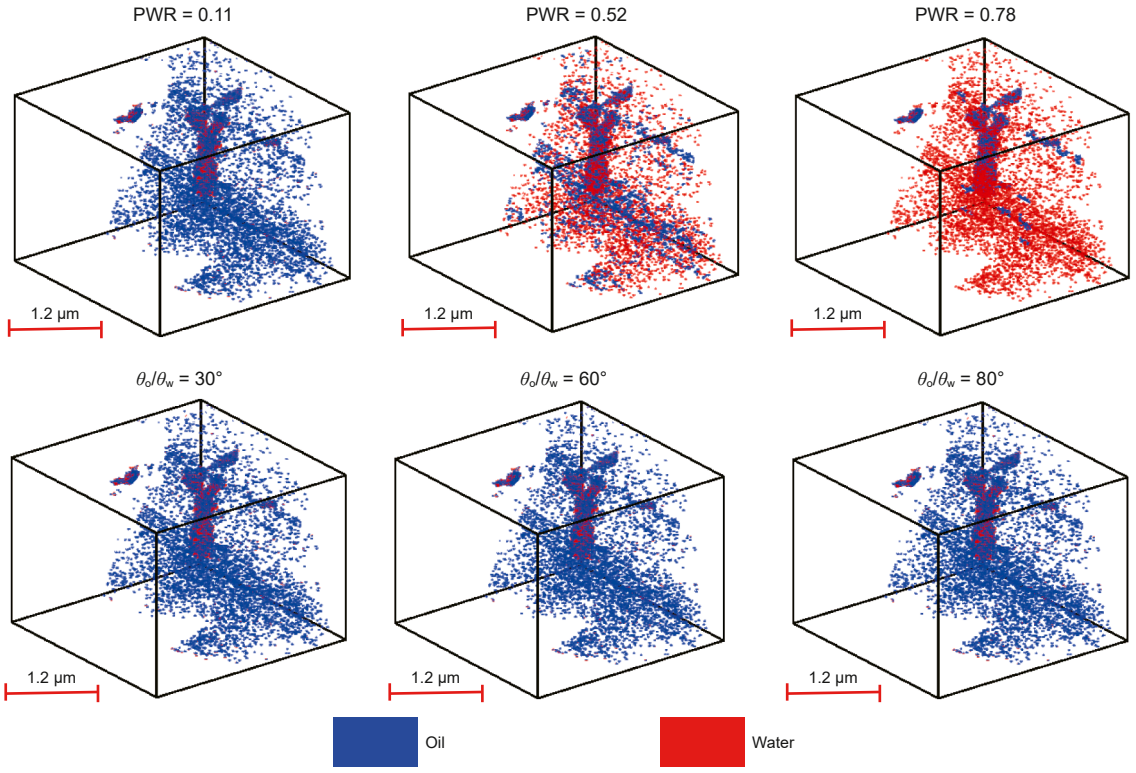


Fig. 4. Fluid distributions in digital shale core at varying proportions of water–wet regions and varying wetting angles. The blue and the red areas represent the three–dimension spatial distribution of oil and water in the inorganic pores, respectively.

T_1 values are compared in Fig. 5(c) and (d), demonstrating excellent agreement.

Based on previous T_2 measurements at different frequencies (Liu et al., 2024a), and the T_1–T_2 experimental results presented in this study, the surface relaxivities and bulk relaxation times for oil and water at 21.36 MHz were established. Subsequently, relying on Eqs. (4)–(5) in Section 2.1, the $\rho_{1S,W}$, $\rho_{1S,O}$, $\rho_{2S,W}$, and $\rho_{2S,O}$ governed the NMR relaxation mechanism at different magnetic field frequencies were determined, as shown in Table 1. In this study, measurements were conducted on shale samples; considering that the T_1 and T_2 of organic matter and pore fluids are influenced by viscosity, separate measurements for these components were not performed.

4.2. Varying proportions of water–wet regions

To investigate the impacts of different PWRs in inorganic pores on T_1–T_2 responses, the random walk method was employed to simulate the saturation recovery–Carr–Purcell–Meiboom–Gill (SR–CPMG) pulse sequence of inorganic pore fluids at varying PWRs (Eqs. (6)–(11)) (Liu et al., 2025a). The T_1–T_2 distributions were obtained using the Butler–Reeds–Dawson (B–R–D) inversion method (Butler et al., 1981), as illustrated in Fig. 6. The results indicate that the increasing proportion of water–wet regions leads to greater water occupancy in large pores within inorganic pores. Consequently, in the T_1–T_2 distribution of inorganic pore fluids, the signal intensity of short relaxation oil decreases, while that of long relaxation water increases. The increasing T_E accelerates the decay rate of echo trains, resulting in decreased signal intensities for both short relaxation oil and long relaxation water distributions (Fig. 6(a), (d), (g); Fig. 6(b), (e), (h); Fig. 6(c), (f), (i)). Furthermore, an increase in magnetic field frequency accelerates the decay rate of echo trains, leading to reduced signal intensities for both short relaxation oil and long relaxation water distributions (Fig. 6(a)–(c); Fig. 6(d)–(f); Fig. 6(g)–(i)). Additionally, the cumulative T_1 distribution shifts toward longer relaxation times due to the frequency dependence of longitudinal surface relaxivity in inorganic pore fluids. The cumulative T_2 distribution is influenced by both the frequency dependence of transverse surface relaxivity and internal magnetic field gradients, shifting left between 21 MHz and 100 MHz, and right between 100 MHz and 200 MHz. It should be noted that we aim to investigate the impact of varying oil and water–wet proportions within inorganic pores on the T_1–T_2 responses. Consequently, signals from fluids in organic pores, organic matter, and clay–bound water in the T_1–T_2 spectrum were not considered. Therefore, certain discrepancies exist between this figure and Fig. 5(b).

4.3. Varying wetting angles

To investigate the impacts of varying wetting angles on T_1–T_2 responses, the random walk method (Liu et al., 2025a) was utilized to simulate SR–CPMG pulse sequences for inorganic pore fluids at varying wetting angles Eqs. (6)–(11). The T_1–T_2 distributions were obtained using the Butler–Reeds–Dawson (B–R–D) inversion method (Butler et al., 1981), as shown in Fig. 7. The results indicate that increasing wetting angle does not significantly alter the distribution of pore fluids within the digital shale core, leading to minimal changes in the T_1–T_2 spectra of inorganic pore fluids. The increasing T_E accelerates the decay rate of echo trains, resulting in reduced signal intensity in the T_1–T_2 distribution of inorganic pore fluids. Moreover, an increase in magnetic field frequency enhances the peak of the cumulative T_1 distribution due to the frequency dependence of surface relaxivities and internal magnetic field gradients, while decreasing the peak of the cumulative T_2 distribution (Liu et al., 2025a). The accelerated decay rate of echo trains

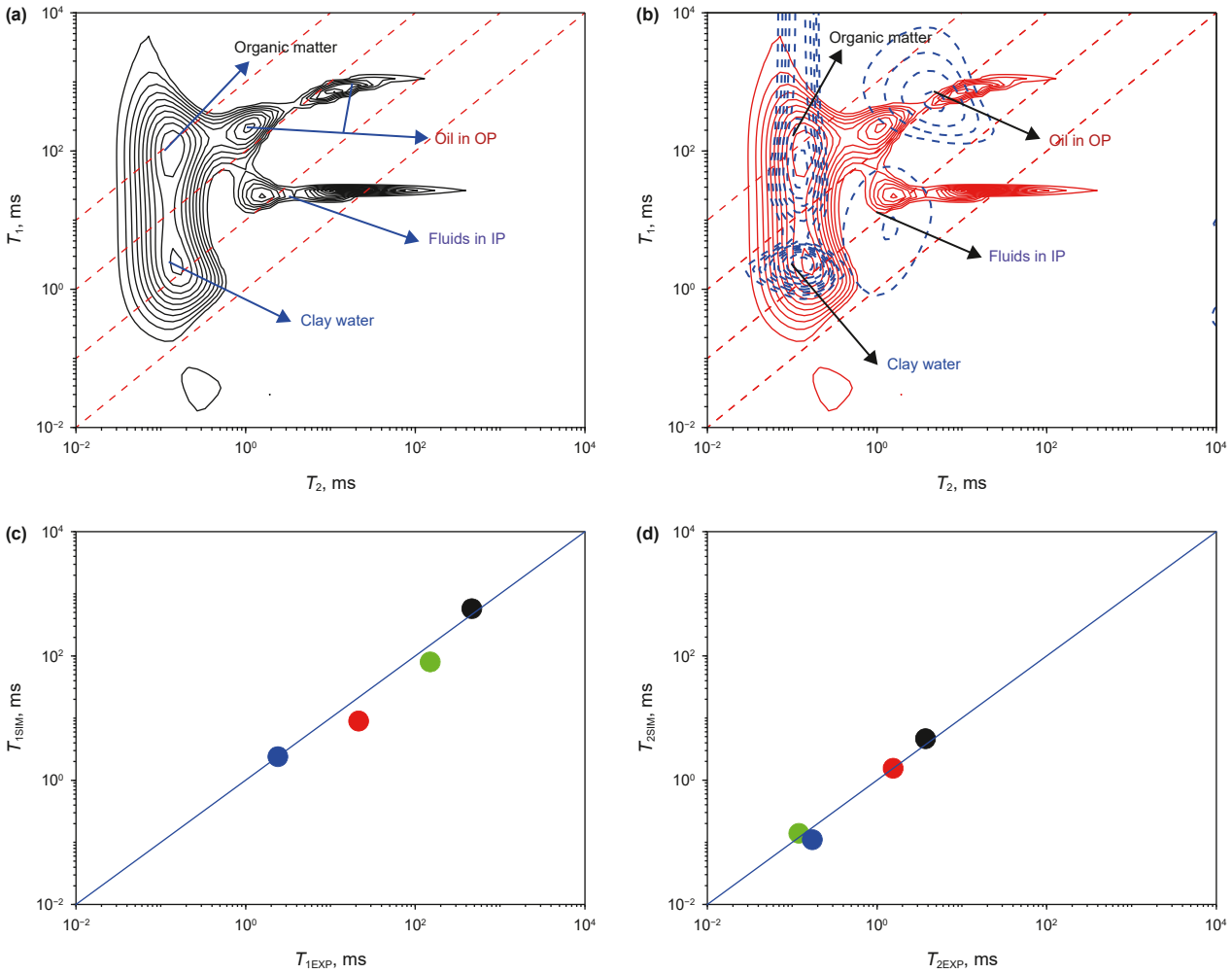


Fig. 5. Verification of T_1–T_2 numerical simulation. **(a)** Experimental results at magnetic field frequency of 21.36 MHz, **(b)** comparisons of experiment and numerical simulation. The blue and red lines represent the numerical simulation and experimental results, **(c)** comparisons of experiment and numerical simulation for T_2 values, **(d)** comparisons of experiment and numerical simulation for T_1 values. In Fig. 5 (b), the red and blue lines represent the T_1–T_2 spectrum for experimental and numerical results. In Fig. 5(c) and (d), the blue, red, green, and black dots represent the T_1 and T_2 values from clay–bound water, water in IP, OM, and oil.

Table 1
Surface relaxavities and bulk relaxation time at different magnetic field frequencies.

Parameters	Fluid types	At different magnetic field frequencies		
		21.36 MHz	100 MHz	200 MHz
ρ_2, μm/s	Oil	6.69	6.57	6.54
	Water	40	34.7	33.3
ρ_1, μm/s	Oil	0.95	0.125	0.088
	Water	6	4.13	3.5
T_{2B}, s	Oil	1.1		
	Water	2.6		

with higher magnetic field frequencies also leads to decreased signal intensity in the T_1–T_2 distribution of inorganic pore fluids.

5. Frequency conversion of petrophysical parameters

Porosity, T_{1LM}, and T_{2LM} are crucial for the physical properties characterization in shale oil. Numerical simulations indicate that there are differences in the NMR responses of inorganic pore fluids in shale oil at different magnetic field frequencies, T_Es, PWRs, and wetting angles. Thus, establishing the frequency conversion relationship of porosity, T_{1LM}, and T_{2LM} is necessary.

5.1. Varying proportions of water–wet regions

5.1.1. Porosity

The results in Fig. 6 demonstrate that varying PWRs in inorganic pore fluids, magnetic field frequencies and T_Es, significantly affect the peak positions and signal intensities of the T_1–T_2 distribution spectra, thereby influencing porosity. It should be noted that the porosity referred to is the porosity measured by NMR instruments, which varies with the instrument's magnetic field frequency, T_E, and fluid distribution. Based on these simulation results, relationships between porosity and frequency were established (Fig. 8). The results demonstrate an increased proportion of water–wet regions leads to larger pore spaces being occupied by water within inorganic pores. In the T_1–T_2 distribution, the signal intensity of short relaxation oil distribution decreases, while that of long relaxation water distribution increases. These changes accelerate the decay rate of echo train, resulting in reduced porosity. For example, at T_E is 0.4 ms, f is 200 MHz, and f_w is 0.78, the porosity is 0.217%, which is 66.7% of the value obtained with a PWR of 0.52. Furthermore, increased magnetic

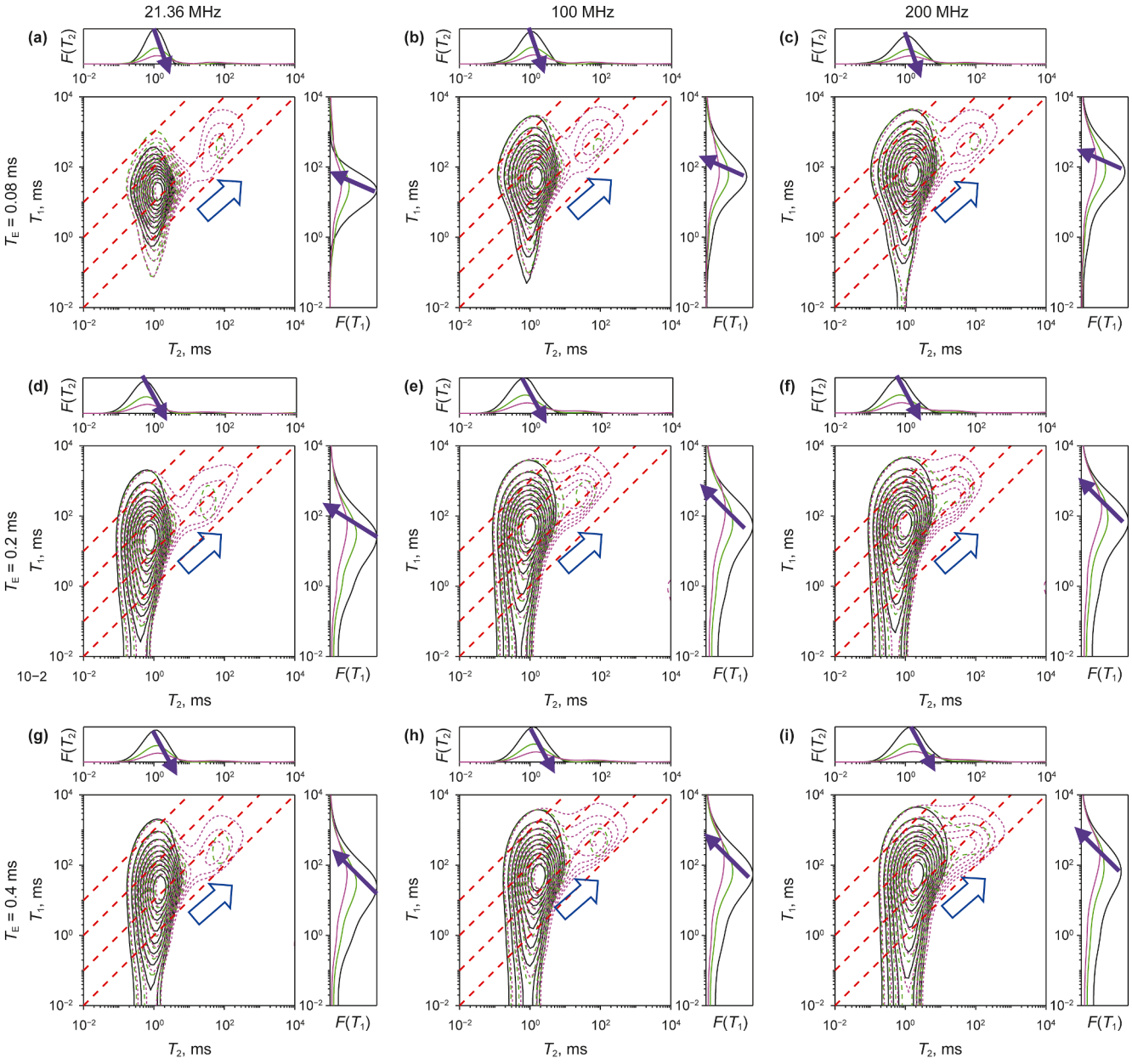


Fig. 6. T_1–T_2 distributions of inorganic pores fluids for water–wet regions with varying proportions and varying T_Es at varying magnetic field frequencies. The black, green, and magenta lines represent the T_1–T_2 distributions when the proportion of water–wet regions in inorganic pores is 0.11, 0.52, and 0.78, respectively.

field frequency accelerates the decay rate of echo trains, reducing porosity. At T_E is 0.4 ms, f is 200 MHz, and f_w is 0.52, the porosity is 0.325%, which is 69.9% of the value obtained at a magnetic field frequency of 21.36 MHz. Similarly, increasing T_E accelerates the decay rate of echo trains, reducing porosity. At T_E is 0.2 ms, f is 200 MHz, and f_w is 0.78, the porosity is 0.253%, which is 1.166 times of that from the T_E with 0.4 ms. Fig. 8 provides the cross–plots for porosity at varying T_Es and PWRs across varying magnetic field frequencies, illustrating the impact of these parameters on porosity.

5.1.2. T_{2LM}

T_{2LM} is related to the distribution of pore size and porosity (Liu et al., 2025b). The numerical simulation results in Fig. 6 demonstrate that varying PWRs, magnetic field frequencies and T_Es affect the spectral peak positions and signal intensities of the T_1–T_2 distribution in inorganic pore fluid. Based on these simulations, the relationships between T_{2LM} and frequency were established at varying proportions of water–wet regions and T_Es (Fig. 9). The results indicate the increasing magnetic field frequency accelerates the decay rate of the echo train. The spectral peak of the T_2 distribution acquired by cumulative T_1 direction of the T_1–T_2 distribution, does not exhibit significant movement, and the degree of reduction in porosity determined the T_{2LM}, which increases. For example, at T_E is 0.4 ms, f is 200 MHz, and f_w is 0.78, the T_{2LM} is 0.354 ms, which is 1.51 times higher than that obtained at a magnetic field frequency of 21.36 MHz. Similarly, increasing T_E accelerates the decay rate of the echo train. The spectral peak of the T_2 distribution acquired by cumulative T_1 direction of the T_1–T_2 distribution does not exhibit significant movement, at this time,

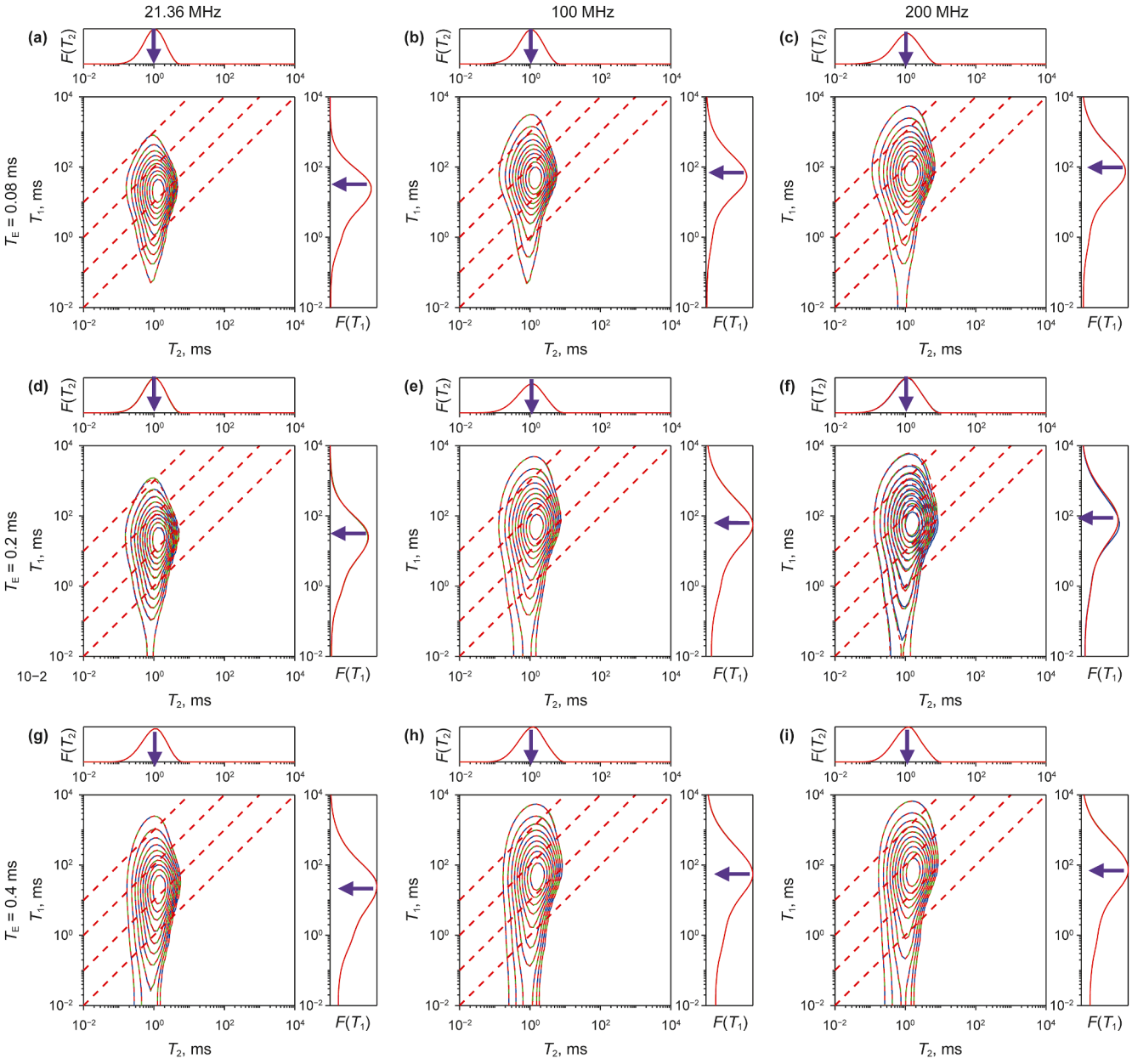


Fig. 7. T_1–T_2 distributions of inorganic pores fluids for varying wet angles and varying T_Es at varying frequencies. The blue, green, and red lines represent the T_1–T_2 distributions of inorganic pore fluids at wetting angles of 30°, 60°, and 80°, respectively.

the degree of reduction in porosity determined the T_{2LM}, which increases T_{2LM}. At $T_E = 0.2$ ms, $f = 200$ MHz, and $f_w = 0.78$, the T_{2LM} is 0.407 ms. It is 1.15 times higher than that obtained at $T_E = 0.4$ ms. As the proportion of water–wet regions increases, the larger pore portions within the inorganic pores are occupied by water. Given the higher transverse surface relaxivity of water compared to oil, this leads to an accelerated decay rate of the echo train. The spectral peak of the T_2 distribution obtained by cumulative T_1 direction of the T_1–T_2 distribution does not exhibit significant movement, at this time, the degree of reduction in porosity determined the T_{2LM}, which increases. At $T_E = 0.4$ ms, $f = 200$ MHz, and $f_w = 0.78$, the $T_{2LM} = 0.354$ ms, which is 1.79 times higher than that obtained with a PWR of 0.52. Fig. 9 provides cross–plots of frequency conversion for varying T_Es and proportions of water–wet regions, illustrating the effects of these parameters on T_{2LM}.

5.1.3. T_{1LM}

T_{1LM} is related to the distribution of pore size and porosity (Liu et al., 2025b), numerical simulations indicate that variations in magnetic field frequency and proportions of water–wet regions affect porosity and peak positions of T_1 distribution. Therefore, establishing the cross–plots is necessary.

The results in Fig. 6 indicate that varying magnetic field frequencies, T_Es, and proportions of water–wet regions significantly affect the spectral peak positions and signal intensities of the T_1–T_2 distributions in inorganic pore fluids. The correction cross–plots for inorganic pore fluid were established based on these findings (Fig. 10). The results imply the increased magnetic field frequency accelerates the decay rate of the echo string, for larger T_E values ($T_E = 0.2$ ms or $T_E = 0.4$ ms), the spectral peaks of the T_1 distribution in the T_2 direction of the T_1–T_2 distribution cumulatively remain stable. The porosity determines the T_{1LM}, which increases.

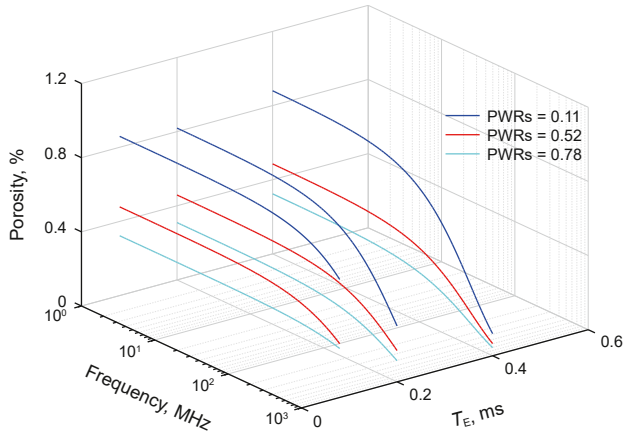


Fig. 8. Porosity–frequency conversions for inorganic pores fluids for varying PWRs and T_Es. The blue, red, and cyan lines represent the frequency conversion of porosity in inorganic pore fluids at varying PWRs.

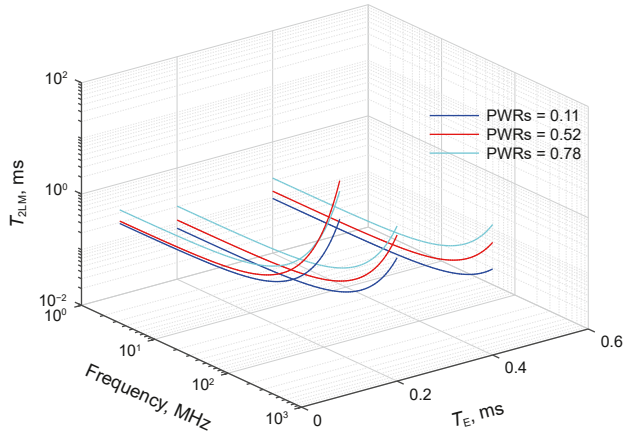


Fig. 9. Frequency conversions of inorganic pores fluids for water–wet regions with varying proportions for varying T_Es. The blue, red, and cyan lines represent the frequency conversion of porosity in inorganic pore for different PWRs.

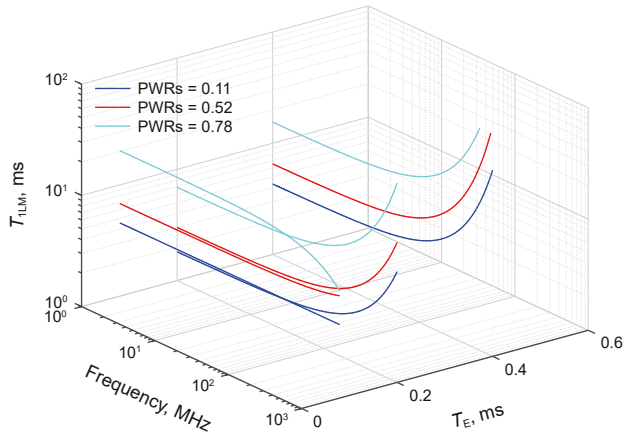


Fig. 10. T_{1LM}–frequency conversions in inorganic pores fluids for varying PWRs. The blue solid, the red solid and the cyan dotted lines represent the frequency conversion of T_{1LM} at varying PWRs, respectively.

For example, for a smaller T_E value (T_E = 0.08 ms), the spectral peaks of the T_1–T_2 distribution in the T_2 direction cumulatively remain stable. At T_E = 0.4 ms, f = 200 MHz, and f_w = 0.78, the T_{1LM} is 27.1 ms, which is 1.65 times higher than that at a magnetic field frequency of 21.36 MHz. For a smaller T_E value (T_E = 0.08 ms), the T_1–T_2 distribution in the T_2 direction cumulatively also remain stable. The porosity decreases to a very low degree, and T_{1LM} increases. Under constant conditions, increasing T_E accelerates the decay rate of the echo train. The spectral peaks of the T_1–T_2 distribution accumulated in both the T_1 and T_2 directions do not shift significantly, and the porosity determines the T_{1LM}, causing it to increase. For example, at T_E = 0.2 ms, f = 200 MHz, and PWR = 0.78, the T_{1LM} is 10.68 ms, 39.4% of that at T_E = 0.4 ms. As the proportion of water–wet regions increases, the larger pores within inorganic pores are occupied by water. Given that the longitudinal surface relaxivity of water is higher than that of oil, which leads to an increase in T_{1LM}. At T_E = 0.4 ms, f = 200 MHz, and PWR = 0.78, the T_{1LM} is 27.1 ms, 2.33 times higher than that at a PWR of 0.52. Fig. 10 provides cross–plots of frequency conversion for varying TEs and proportions of water–wet regions, illustrating the effects of these parameters on T_{1LM}.

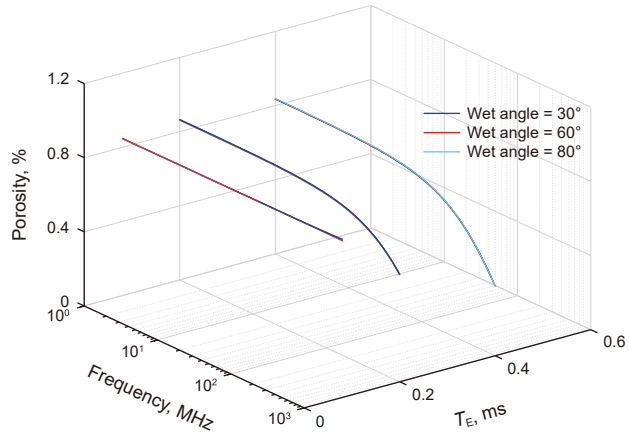


Fig. 11. Porosity–frequency conversion for inorganic pores fluids with varying wet angles at varying T_Es. The blue, red, and cyan lines represent the porosity–frequency conversion in inorganic pore fluid at varying wet angles, respectively.

5.2. Varying wet angles

5.2.1. Porosity

The numerical simulation in Fig. 7 show that varying wet angles, magnetic field frequencies, and T_Es significantly affect the spectral peak positions and signal intensities of the T_1–T_2 distribution in the inorganic pore fluid. Based on these results, the frequency conversion cross–plots for porosity at varying wet angles and T_Es were established (Fig. 11). The findings indicate that increasing magnetic field frequency accelerates the decay rate of the echo train, leading to the decreased porosity. For example, T_E = 0.4 ms, f = 200 MHz, and θ_A = 80°, the porosity is 0.714%, which is 86.6% of that observed at a magnetic field frequency of 21.36 MHz. Similarly, If the increasing T_E accelerates the decay rate of the echo train, resulting in the decreased porosity. At T_E = 0.2 ms, f = 200 MHz, and θ_A = 80°, the porosity is 0.795%, which is 1.11 times higher than that obtained at T_E = 0.4 ms. In contrast, increasing wet angle does not significantly alter porosity due to minimal changes in the number of voxels occupied by inorganic pore fluids. For instance, at T_E = 0.4 ms, f = 200 MHz, and θ_A = 80°, the porosity is 0.713%, which is 1 times of that obtained with a wetting angle of 60°. Fig. 11 provides cross–plots illustrating the relationships between frequency and porosity at varying T_Es and wet angles.

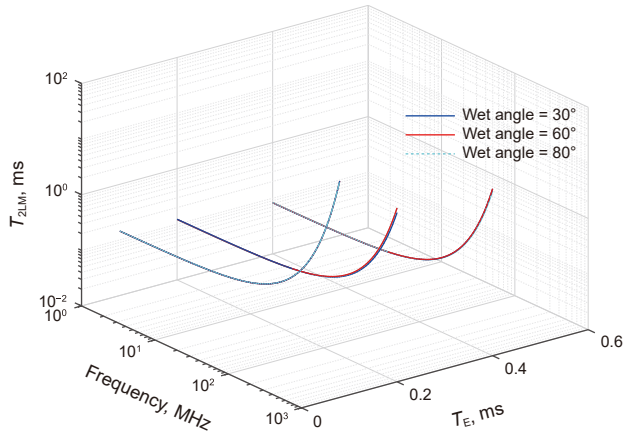


Fig. 12. T_{2LM}–frequency conversions of inorganic pores fluids with varying wetting angles for varying T_Es. The blue, red and cyan lines represent the frequency conversion of T_{2LM} at varying T_Es and wetting angles.

5.2.2. T_{2LM}

The results in Fig. 7 imply the varying wet angles at different magnetic field frequencies and T_Es affect the spectral peaks positions and the signal intensities of the T_1–T_2 distribution in the inorganic pores. Frequency conversion cross–plots for varying wet angles and T_Es were established based on these findings (Fig. 12). The results imply the increased magnetic field frequency and T_E accelerate the attenuation rate of the echo train. However, the spectral peaks of the T_2 distribution accumulated in the T_1 direction of the T_1–T_2 distribution remain stable, which is determined by the porosity, and T_{2LM} increases. At $T_E = 0.4$ ms, $f = 200$ MHz, and $\theta_A = 80°$, the T_{2LM} is 0.214 ms, which is 2.33 times higher than that at a magnetic field frequency of 21.36 MHz. In contrast, increasing the wet angle does not significantly alter the decay rate of the echo train. The spectral peaks of the T_2 distribution accumulated in the T_1 direction of the T_1–T_2 distribution also remain stable, with no significant changes observed. For instance, at $T_E = 0.4$ ms, $f = 200$ MHz, and a wetting angle of 80°, the porosity is 0.213%, which is 98% of that at a wet angle of 60°. Fig. 12 provides cross–plots illustrating the relationships between frequency and T_{2LM} for varying T_Es and wet angles.

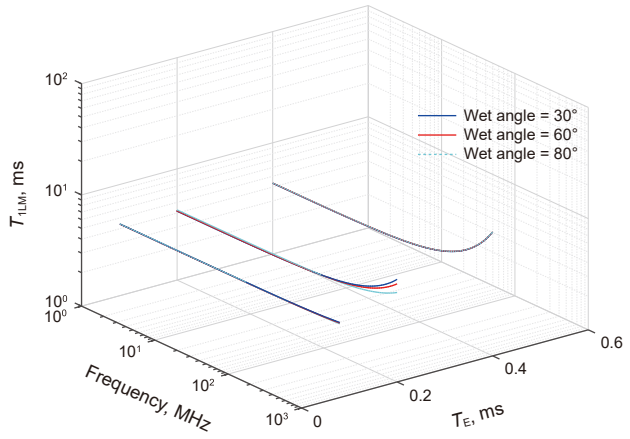


Fig. 13. T_{1LM}–frequency conversions of inorganic pores fluids with varying wet angles for varying T_Es. The blue, red and cyan lines represent the frequency conversion of T_{1LM} at varying T_Es and wet angles.

5.2.3. T_{1LM}

The results in Fig. 7 imply that the varying wet angles have small effects on the spectral peak positions and signal intensities of the T_1–T_2 distribution in the inorganic pores, whereas variations in magnetic field frequency and T_E significantly influence these parameters. Frequency conversion cross–plots for varying wet angles and T_Es were established based on these findings (Fig. 13). Increasing magnetic field frequency accelerates the decay rate of the echo train, but the spectral peaks of the T_1–T_2 distribution in the T_2 direction do not shift significantly. Any observed increases are determined by porosity. For example, at $T_E = 0.4$ ms, $f = 200$ MHz, and a wet angle of 80°, the T_{1LM} is 5.41 ms, which is 1.22 times higher than that obtained at a magnetic field frequency of 21.36 MHz. Similarly, increasing T_E accelerates the decay rate of the echo train, with the spectral peaks of the T_1 distribution in the T_2 direction remaining stable. The increasing T_{1LM} is determined by porosity. At $T_E = 0.2$ ms, $f = 200$ MHz, and a wetting angle of 80°, the T_{1LM} is 4.63 ms, which is 85.5% of that obtained at $T_E = 0.4$ ms. An increasing wetting angle of inorganic pore fluids does not significantly alter the attenuation rate of the echo train due to minimal changes in the number of fluid voxels within the inorganic pores. Consequently, the spectral peaks of the T_1 distribution accumulated in the T_2 direction to acquire the T_1 distribution do not shift significantly, and no significant changes are observed. For example, at $T_E = 0.4$ ms, $f = 200$ MHz, and a wetting angle of 80°, the T_{1LM} is 5.414 ms, which is essentially unchanged from that obtained at a wetting angle of 60°. Fig. 13 provides cross–plots illustrating the relationships between frequency and T_{1LM} for varying T_Es and inorganic pore wet angles.

6. Discussion

Shale oil reservoirs exhibit highly complex fluid behavior, making the study of NMR relaxation theory particularly challenging. To elucidate the NMR response mechanisms in shale oil reservoirs, we developed a T_1–T_2 response simulation technique and a frequency conversion methodology based on three–dimensional digital cores in mixed–wet shale oil. Nevertheless, several limitations remain that require further improvement in future work.

First, there is an issue regarding the derivation of fluid surface relaxivity based on cylindrical pore assumptions. In the theory section, cylindrical pores are used to simplify the complex pore structure for deriving the analytical expression of fluid surface relaxivity, which is then calibrated by NMR experiments. The derived surface relaxivity represents an average value and does not account for the influence of the actual complex pore networks. In future studies, we will consider assigning a distinct surface relaxivity value to each voxel within the pore space to achieve more accurate determination of fluid surface relaxivity in the intricate pore geometry of shale oil reservoirs.

Second, there is the issue of representativeness of the three–dimensional digital core. Fluids in downhole shale oil reservoirs predominantly reside in micro– and nano–scale pores. The small–sized digital core used in this study (200 × 200 × 200 voxels, 3.9 μm^3) aligns with this geological characteristic and thus possesses a certain degree of representativeness. Numerical simulations of NMR response mechanisms based on this core can therefore provide meaningful insights into NMR behavior of shale oil reservoirs. Moreover, while the heterogeneous oil saturation distribution in shale affects the signal intensity (high or low) in the T_1–T_2 spectrum, it has limited impact on the position of fluid signals within the spectrum. We will incorporate actual downhole T_1–T_2 spectral from shale oil reservoirs to further investigate NMR response mechanisms in future work.

Third, model validation remains insufficient. We have already conducted T_2 measurements on shale plug samples at different frequencies (Liu et al., 2024a). However, for T_1–T_2 measurements, our preliminary experiments—including oil extraction, salt removal, and oil re–saturation—revealed that shale plug samples are extremely prone to fracturing, making it difficult to reliably validate the frequency conversion relationships. In future research, we plan to optimize experimental protocols to enable robust validation frequency–dependent of petrophysical parameters.

Fourth, the observed weak variations in the T_1–T_2 spectra with changing contact angles require further investigation. Our prior characterization of the three–dimensional digital core, focusing on pore connectivity, heterogeneity, and pore–size distribution, indicated that this core features poor pore connectivity, strong heterogeneity, and a narrow pore–size distribution (Liu et al., 2023). In this study, we found that the number of fluid–occupied voxels changes only slightly with contact angle, suggesting that the disconnected pore geometry dominates the NMR response, thereby minimizing spectral shifts in T_1–T_2. In future work, we will conduct dedicated wettability measurement experiments to systematically establish the relationship between wettability variations and T_1–T_2 responses in three–dimensional digital shale cores. Additionally, we plan to refine the digital core by increasing its spatial resolution, thereby enabling more detailed investigations into NMR response mechanisms in shale oil reservoirs.

Fifth, experimental instruments operating at magnetic field frequencies of 100 MHz and 200 MHz are currently unavailable in China. Our experimental results have been validated using instruments at 2 MHz and 21.36 MHz. Given the opportunity in the future, we also intend to validate these results using instruments operating at 100 MHz or 200 MHz.

7. Conclusions

The complexity of the fluid storage states in shale oil and the frequency differences between NMR measurement instruments and NMR logging can affect the T_1–T_2–based petrophysical characterization in shale oil. Numerical simulation techniques are able to quantify the effects from single factors on the petrophysical characteristics. In this paper, we proposed the T_1–T_2 relaxation theory and numerical investigation for T_1–T_2 responses in mixed–wetted shale oil. With the numerical simulation results of T_1–T_2 experimental calibration of digital cores, the T_1–T_2 responses of the mixed wetting shale oil reservoir were simulated for the first time by the random walk algorithm, which reveals the T_1–T_2 response mechanism of the mixed–wetted shale oil reservoir at different magnetic field frequencies. The following conclusions were drawn.

(1) The proposed T_1–T_2 relaxation theory in mixed–wetted shale oil is able to characterize the complex fluid storage state of shale oil reservoirs, and can provide new insights into the T_1–T_2–based petrophysical characterization of the fluid components and the frequency–independent of the petrophysical parameters acquired from NMR measurement instruments and NMR logging in mixed–wetted shale oil.

(2) The T_1–T_2 responses of mixed–wet shale oil reservoirs are complex, the effects from proportions of water–wet regions on T_1–T_2 responses are stronger than that of the wetting angles. If the proportion of water–wet regions increases, the large pores in the inorganic pore space are occupied by water. In the T_1–T_2 distribution, the signal intensity of the short relaxation for oil distribution decreases, and the signal intensity of the long relaxation for water distribution increases. The decay rate of the echo is accelerated, leading to a decreased porosity. The increases of the magnetic field frequency and T_E can accelerate the decay rate of the echo, and the porosity decreases.

(3) The proportion of water–wet regions, magnetic field frequency and T_E have greater effects on porosity. When T_E is 0.4 ms, f is 200 MHz, and PWR is 0.78, the porosity is 0.217%. It is 66.7% of that from the proportion of water–wet regions with 0.52. When T_E is 0.4 ms, f is 200 MHz, and PWR is 0.52, the porosity is 0.325%. It is 69.9% of that from the magnetic field frequency with 21.36 MHz. When T_E is 0.2 ms, f is 200 MHz, and PWR is 0.78, the porosity is 0.253%. It is 1.166 times of that from the T_E with 0.4 ms. The proportion of water–wet regions, magnetic field frequency and T_E have greater effects on T_{2LM}. When T_E is 0.4 ms, f is 200 MHz, and PWR is 0.78, the T_{2LM} is 0.354 ms. It is 1.51 times of that from the magnetic field frequency with 21.36 MHz. When T_E is 0.2 ms, f is 200 MHz, and PWR is 0.78, the T_{2LM} is 0.407 ms. It is 1.15 times of that from the T_E with 0.4 ms. When T_E is 0.4 ms, f is 200 MHz, and PWR is 0.78, the T_{2LM} is 0.354 ms. It is 1.79 times of that from the proportion of water–wet regions with 0.52. The proportion of water–wet regions, magnetic field frequency and T_E have greater effects on T_{1LM}. When T_E is 0.4 ms, f is 200 MHz, and PWR is 0.78, the T_{1LM} is 27.1 ms. It is 1.65 times of that from the magnetic field frequency with 21.36 MHz. When T_E is 0.2 ms, f is 200 MHz, and PWR is 0.78, the T_{1LM} is 10.68 ms. It is 39.4% of that from the T_E with 0.4 ms.

The proposed method provides new insights into the NMR–based petrophysical characterization of mixed wetting shale oil reservoirs and frequency conversion of petrophysical parameters based on NMR measurement instrumentation and NMR logging. These findings contribute to the accurate evaluation of shale oil reservoirs.

CRediT authorship contribution statement

Ji-Long Liu: Writing – original draft, Visualization, Validation, Software, Resources, Methodology, Investigation, Funding acquisition, Formal analysis, Data curation, Conceptualization. **Ran-Hong Xie:** Writing – review & editing, Supervision, Project administration. **Jiang-Feng Guo:** Writing – review & editing, Visualization, Validation, Software, Resources, Methodology. **Bo-Chuan Jin:** Methodology, Software. **Chong Deng:** Data curation, Conceptualization.

Declaration of competing interest

The authors declare that they have no known competing financial interests or personal relationships that could have appeared to influence the work reported in this paper.

Acknowledgements

This work was funded by the National Natural Science Foundation of China (No. 42174131).

References

Al–Garadi, K., El–Husseiny, A., Elsayed, M., et al., 2022. A rock core wettability index using NMR T_2 measurements. Journal of Petroleum Science and Engineering 208, 109386. https://doi.org/10.1016/j.petrol.2021.109386.

Al–Mahrooqi, S.H., Grattoni, C.A., Moss, A.K., et al., 2003. An investigation of the effect of wettability on NMR characteristics of sandstone rock and fluid systems. Journal of Petroleum Science and Engineering 39, 389–398. https://doi.org/10.1016/S0920–4105(03)00077–9.

Al–Mahrooqi, S.H., Grattoni, C.A., Muggeridge, A.H., et al., 2006. Pore–scale modelling of NMR relaxation for the characterization of wettability. Journal of Petroleum Science and Engineering 52, 172–186. https://doi.org/10.1016/j.petrol.2006.03.008.

Al–Muthana, A.S., Hursan, G.G., Ma, S.M., et al., 2012. Wettability as a Function of Pore Size by NMR. Presented in Aberdeen, Scotland, UK. https://jgmaas.com/SCA/2012/SCA2012–31.

Bonalde, I., Martín-Landrove, M., Benavides, A., et al., 1995. Nuclear magnetic resonance relaxation study of wettability of porous rocks at different magnetic fields. Journal of applied physics 78, 6033–6038. https://doi.org/10.1063/1.360541.

Borgia, G.C., Fantazzini, P., Mesini, E., 1991. Wettability effects on oil-water-configurations in porous media: a nuclear magnetic resonance relaxation study. Journal of applied physics 70, 7623–7625. https://doi.org/10.1063/1.349720.

Brown, R.J.S., Fatt, I., 1956. Measurements of Fractional Wettability of Oil Fields' Rocks by the Nuclear Magnetic Relaxation Method. Presented in Fall Meeting of the Petroleum Branch of AIME. https://doi.org/10.2118/743–G.

Butler, J.P., Reeds, J.A., Dawson, S.V., 1981. Estimating solutions of first kind integral equations with nonnegative constraints and optimal smoothing. SIAM J NUMER ANAL 18, 381–397. https://doi.org/10.1137/0718025.

Chen, J., Hirasaki, G.J., Flaum, M., 2006. NMR wettability indices: effect of OBM on wettability and NMR responses. Journal of Petroleum Science and Engineering 52, 161–171. https://doi.org/10.1016/j.petrol.2006.03.007.

Dick, M.J., Veselinovic, D., Bonnie, R.J.M., et al., 2022. NMR–based wettability index for unconventional rocks. Petrophysics 63 (3), 418–441. https://doi.org/10.30632/PJV63N3–2022a9.

Fleury, M., Deflandre, F., 2003. Quantitative evaluation of porous media wettability using NMR relaxometry. Magnetic resonance imaging 21, 385–387. https://doi.org/10.1016/S0730–725X(03)00145–0.

Gao, Z., Bai, L., Hu, Q., et al., 2024. Shale oil migration across multiple scales: a review of characterization methods and different patterns. Earth–Science Reviews 254, 104819. https://doi.org/10.1016/j.earscirev.2024.104819.

Guan, H., Brougham, D., Sorbie, K.S., et al., 2002. Wettability effects in a sandstone reservoir and outcrop cores from NMR relaxation time distributions. Journal of Petroleum Science and Engineering 34, 35–54. https://doi.org/10.1016/S0920–4105(02)00151–1.

Hirasakl, G.J., 1991. Wettability: fundamentals and surface forces. SPE formation evaluation 6, 217–226. https://doi.org/10.2118/17367–PA.

Howard, J.J., 1998. Quantitative estimates of porous media wettability from proton NMR measurements. Magn. Reson. Imaging 16, 529–533. https://doi.org/10.1016/S0730–725X(98)00060–5.

Hsu, W.F., Li, X., Flumerfelt, R.W., 1992. Wettability of porous media by NMR relaxation methods. In: Presented in the 67th Annual Technical Conference and Exhibition of the Society of Petroleum Engineers. https://doi.org/10.2118/24761–MS.

Kumar, J., Fatt, I., Saraf, D.N., 1969. Nuclear magnetic relaxation time of water in a porous medium with heterogeneous surface wettability. J. Appl. Phys. 40, 4165–4171. https://doi.org/10.1063/1.1657160.

Liang, C., Xiao, L., Zhou, C., et al., 2019. Two–dimensional nuclear magnetic resonance method for wettability determination of tight sand. Magnetic resonance imaging 56, 144–150. https://doi.org/10.1016/j.mri.2018.09.020.

Liang, C., Xiao, L., Jia, Z., et al., 2023. Mixed wettability modeling and nuclear magnetic resonance characterization in tight sandstone. Energy & Fuels 37, 1962–1974. https://doi.org/10.1021/acs.energyfuels.2c03720.

Lipari, G., Szabo, A., 1982. Model–free approach to the interpretation of nuclear magnetic resonance relaxation in macromolecules. 1. Theory and range of validity. J. Am. Chem. Soc. 104, 4546–4559. https://doi.org/10.1021/ja00381a009.

Liu, J., Xie, R., Guo, J., et al., 2023. Multicomponent digital core construction and three–dimensional micro–pore structure characterization of shale. Physics of Fluids 35, 082003. https://doi.org/10.1063/5.0155425.

Liu, J., Xie, R., Guo, J., et al., 2024a. Study of nuclear magnetic resonance response mechanism in shale oil and correction of petrophysical parameters. Fuel 358, 130162. https://doi.org/10.1016/j.fuel.2023.130162.

Liu, J., Xie, R., Guo, J., 2024b. Pore–scale T_2–based numerical investigation on dynamics and wettability in mixed–wet shale oil reservoirs. Physics of Fluids 36, 122025. https://doi.org/10.1063/5.0247232.

Liu, J., Xie, R., Guo, J., 2024c. Numerical investigation of T_2^*–based and T_2–based petrophysical parameters frequency–dependent in shale oil. Energy 313, 133788. https://doi.org/10.1016/j.energy.2024.133788.

Liu, J., Xie, R., Guo, J., et al., 2025a. Numerical investigation on 2–D NMR response mechanisms and the frequency conversion of petrophysical parameters in shale oil reservoirs. Pet. Sci. 5, 1959–1976. https://doi.org/10.1016/j.petsci.2025.03.014.

Liu, J., Xie, R., Guo, J., et al., 2025b. Numerical investigations on T_1–T_2^*–based petrophysical evaluation in shale oil reservoir with complex minerals. Pet. Sci. 22 (11), 4538–4554. https://doi.org/10.1016/j.petsci.2025.07.020.

Looyestijn, W., Hofman, J., 2006. Wettability–index determination by nuclear magnetic resonance. SPE Reservoir Evaluation & Engineering 9, 146–153. https://doi.org/10.2118/93624–PA.

Looyestijn, W.J., 2008. Wettability index determination from NMR logs. Petrophysics 49, 130–145. https://onepetro.org/petrophysics/article–abstract/171141.

Mi, S., Guo, Q., Zhang, Q., et al., 2023. Classification and potential of continental shale oil resources in China and resource evaluation methods and criteria. Oil Shale 40 (4), 283–320. https://doi.org/10.3176/oil.2023.4.02.

Newgord, C., Tandon, S., Heidari, Z., 2020. Simultaneous assessment of wettability and water saturation using 2D NMR measurements. Fuel 270, 117431. https://doi.org/10.1016/j.fuel.2020.117431.

Pang, X., Li, M., Li, B., et al., 2023. Main controlling factors and movability evaluation of continental shale oil. Earth–Science Reviews 243, 104472. https://doi.org/10.1016/j.earscirev.2023.104472.

SayedAkram, N.I., Shikhov, I., Arns, J.Y., et al., 2016. Micro–CT assisted interpretation of NMR responses of heterogeneous mixed–wet carbonate rock. In: the SPWLA 57th Annual Logging Symposium. Reykjavik, Iceland. https://SPWLAALS/proceedingsabstract/SPWLA–2016–QQQ/28618.

Singer, P.M., Valiya Parambathu, A., Wang, X., et al., 2020. Elucidating the ^{1}H NMR relaxation mechanism in polydisperse polymers and bitumen using measurements, MD simulations, and models. J. Phys. Chem. B 124, 4222–4233. https://pubs.acs.org/doi/10.1021/acs.jpcb.0c01941.

Su, S., Jiang, Z., Shan, X., et al., 2018. The wettability of shale by NMR measurements and its controlling factors. Journal of Petroleum Science and Engineering 169, 309–316. https://doi.org/10.1016/j.petrol.2018.05.067.

Sulucarnain, I., Sondergeld, C.H., Rai, C.S., 2012. An NMR study of shale wettability and effective surface relaxivity. In: Presented in the SPE Canadian Unconventional Resources Conference. https://doi.org/10.2118/162236–MS. Calgary, Alberta, Canada.

Tandon, S., Heidari, Z., 2019. Quantifying the mechanisms contributing to nuclear–magnetic–resonance surface relaxation of protons in kerogen pores of organic–rich mudrocks. SPE J. 24, 2438–2457. https://doi.org/10.2118/197063–PA.

Tandon, S., Newgord, C., Heidari, Z., 2020. Wettability quantification in mixed–wet rocks using a new NMR–based method. SPE Reservoir Evaluation & Engineering 23, 896–916. https://doi.org/10.2118/191509–PA.

Valori, A., Hursan, G., Ma, S.M., 2017. Laboratory and downhole wettability from NMR T_1/T_2 ratio. Petrophysics 58, 352–365. https://petrophysics/article–abstract/58/04/352/179388.

Valori, A., Ali, F., Abdallah, W., 2018. Downhole wettability: the potential of NMR. In: Presented in the SPE EOR Conference at Oil and Gas West Asia. Muscat, Oman. https://doi.org/10.2118/190332–MS.

Wang, X., Wang, M., Li, J., et al., 2022. Thermal maturity: the controlling factor of wettability, pore structure, and oil content in the lacustrine Qingshankou shale, Songliao Basin. Journal of Petroleum Science and Engineering 215, 110618. https://doi.org/10.1016/j.petrol.2022.110618.

Wang, L., Yin, R., Sima, L., et al., 2018. Insights into pore types and wettability of a shale gas reservoir by nuclear magnetic resonance: Longmaxi Formation, Sichuan Basin, China. Energy & fuels 32, 9289–9303. https://doi.org/10.1021/acs.energyfuels.8b02107.

Zhao, W., Bian, C., Li, Y., et al., 2023. Enrichment factors of movable hydrocarbons in lacustrine shale oil and exploration potential of shale oil in Gulong Sag, Songliao Basin, NE China. Pet Explor Dev 50 (3), 520–533. https://doi.org/10.1016/S1876–3804(23)60407–0.

Zou, C., Yang, Z., Zhang, G., et al., 2023. Theory, technology and practice of unconventional petroleum geology. J Earth Sci 34 (4), 951–965. https://doi.org/10.1007/s12583–023–2000–8.

Zou, C., Yang, Z., Li, G., et al., 2022. Why can China realize the continental “shale oil revolution”? J Earth Sci 33 (5), 1324–1327. https://doi.org/10.1007/s12583–022–1745–7.

Zou, C., Yang, Z., Cui, J., et al., 2013. Formation mechanism, geological characteristics and development strategy of nonmarine shale oil in China. Petrol. Explor. Dev 40, 15–27. https://doi.org/10.1016/S1876–3804(13)60002–6.